Experiments in Fluids (2006) 41: 365–373
DOI 10.1007/s00348-006-0135-8

RESEARCH ARTICLE

Yi-Chun Wang · Ching-Hung Huang
Yung-Chun Lee · Ho-Hsun Tsai

Development of a PVDF sensor array for measurement of the impulsive pressure generated by cavitation bubble collapse

Received: 5 December 2005 / Revised: 7 March 2006 / Accepted: 13 March 2006 / Published online: 23 June 2006

Abstract To study the impulsive pressure generated by cavitation bubble collapse, a PVDF piezoelectric array of pressure sensors is developed. The sensor array is fabricated directly on a 25 μm thick aluminum-metalized polarized PVDF film using a laser micro-machining technique. Dynamic calibration of the sensor array is accomplished in a gas shock tube. The average response time of the PVDF sensors to the fast-rising gas dynamic shock is found as fast as 31 ns. The array sensor is then attached on the solid boundary attacked by the collapse of the bubble. The features and the possible mechanisms of the impulsive pressure are discussed. The high sensitivity, low crosstalk, and low cost of the PVDF sensor array indicates its applicability in high amplitude impulsive field measurements.

1 Introduction

The primary motivation for this work is to develop an array of sensors which can be used to simultaneously measure the spatial distribution and the temporal variation of an impulsive pressure field such as that generated by the collapse of a cavitation bubble. It is well known that cavitation bubble collapse is very destructive, causing extremely large noise and material erosion on nearby solid surfaces. Experiments have indicated that a collapsing bubble (no matter it collapses spherically or the collapse is perturbed by any asymmetric cause such as the presence of boundaries) always emits shock waves, which are generally characterized by high amplitude and very short duration of time (see, for example, Jones and Edwards 1960; Vogel and Lauterborn 1988). Indeed, Vogel et al. (1989) reported that the acoustic transients emitted upon the spherical bubble collapse have duration of 20–30 ns, much shorter than the rise time of most pressure transducers commercially available. Significant errors can occur if one uses these transducers to measure the pressure pulses. These facts lead to the demand of developing pressure sensors that have high bandwidth and durability in order to record the actual values of the short pressure pulses.

The amplitude and the duration of the impulsive pressure produced from a collapsing bubble are mainly affected by the stand-off parameter $\gamma \equiv L/R_{\max}$ (see, for example, Tomita and Shima 1986), where L is the initial distance of the bubble from the boundary and $R_{\max}$ is the maximum bubble radius. Although at least three mechanisms of impulsive pressure generation, namely the shock wave, the impinging liquid jet, and the splashing effect, have been identified (see, for example, Brennen 1995; Tong et al. 1999 and the references therein), a quantitative relationship between the pressure pulses and these mechanisms is still incomplete due to the extremely fast and complicated unsteady flow phenomena; the processes happen so quickly that very high-speed photography is necessary to offer enough temporal resolution. Furthermore, the collapse events are covered by the bubble wall and are very difficult to visualize.

Recently, Brujan et al. (2002) investigated the final stage of collapse of a laser-generated bubble close to a rigid boundary using high-speed photography of maximum framing rate up to 5 million frames/s. They focused on the bubble stand-off parameter $\gamma \approx 1$ and pictured emission of multiple shock waves after the liquid jet penetrates the bubble, splashes away from the solid boundary, and leads to the formation of two toroidal cavities split from the main bubble. Equipped with an extra high-speed camera of maximum framing rate of 100 million frames/s, Lindau and Lauterborn (2003) observed very complex bubble collapse scenarios near a wall. They visualized shock waves originated from different flow dynamic mechanisms for the case of

Y.-C. Wang (✉) · C.-H. Huang · Y.-C. Lee · H.-H. Tsai
Department of Mechanical Engineering,
National Cheng Kung University, Tainan 701, Taiwan
E-mail: wangyc@mail.ncku.edu.tw
Tel.: +886-6-2757575
Fax: +886-6-2352973

$\gamma = 2.6$ by employing a shadowgraph illumination. They also reported the photographic records of the bubble dynamics for lower values of γ between 1.2 and 0.1. Since one of the most important consequences of cavitation is its erosion on nearby boundaries, the lack of direct measurement of the impulsive pressure generated by bubble collapse with enough temporal and spatial resolution is considered to be a shortcoming of the previous work.

To explore the composition of the impulsive pressure generated by the cavitation bubble collapse, we design and construct a sensor array on a 25 μm thick PVDF (polyvinylidene fluoride) piezoelectric film using a laser micro-fabrication technique. There are several reasons for choosing PVDF film in the present study. The film has natures of non-perturbing (thin and flexible) structure, good durability, high response frequency, large range of linearity, and, most importantly, low acoustic impedance (compared to piezoceramics). This close match of impedance permits more efficient transduction of acoustic signal in water and assures excellent sensitivity and high bandwidth. These properties have made it an ideal sensor material for medical ultrasonic measurements (see, for example, Harris and Lewin 1999) and in cavitation research, as demonstrated recently by Arndt et al. (1997), Soyama et al. (1998), and Shaw et al. (2000).

In the following, design and fabrication of the array of sensors are described first. Dynamic calibration of the sensor using a gas shock tube is then demonstrated. Finally, the pressure pulses emitted by cavitation bubble collapse for few selected values of γ are presented. Possible fluid dynamic mechanisms responsible for these pressure pulses are also discussed.

2 Design and fabrication of PVDF sensor array

2.1 Fabrication of sensor array

The sensor array is fabricated directly on a 25 μm thick aluminum-metalized polarized PVDF film (FV301926, Goodfellow Cambridge Ltd, UK) using an excimer laser micro-machining system (PS-2000, Excitech Ltd, Oxford, UK). As illustrated in Fig. 1, the laser system emits KrF ultraviolet light pulses with energies up to 350 mJ and pulse duration of 30 ns. After passing a mask, the laser beam is modulated in shape and size and is focused onto the target surface (the aluminum electrode of the PVDF film) using a 10× projection optics. Instant ablation of the metal electrode occurs due to localized absorption of the high-density laser energy. The position and path of the laser beam relative to the target surface are controlled using a PC-based programmable x–y–z precision stage (with resolution of 1 μm). The personal computer also triggers the laser to ensure the synchronization between the laser pulses (with repetition rate ranging from 1 to 100 Hz) and the stepwise servo-motion of the precision stage. The maximum laser fluency delivered on the target surface can approximately be 2 mJ/cm^2. Combination of several machining parameters, including the pulse energy, degree of energy attenuator, and pulse repetition rate, is carefully selected such that the laser only removes the top electrode of the film and keeps the bottom one intact. The smallest dimension of the focusing laser beam is 10 μm, enough for accurate patterning of the electrodes.

Plotted in Fig. 2 is the layout of the PVDF sensor array. A row of four independent sensing elements is patterned on the film. The sensitive area is formed by overlapping isolated electrodes from both sides. As subjected to dynamic pressure, electrical potentials only between overlapping electrodes can be extracted. The size of the sensing elements is 4.8×4.8 mm^2, and the spacing between centers of these elements is 6.4 mm.

2.2 Design of the buffer circuit

The theoretical quarter wavelength resonance frequency of the present 25 μm PVDF film is about 22 MHz (in thickness mode). As operating below its resonant frequency, a piezoelectric element is basically a capacitor. The capacitance of the PVDF piezo film is proportional to its permittivity (about 12) and surface area and is inversely proportional to its thickness. If the piezo film is modeled as a voltage generator, the capacitance can be regarded as equivalent impedance in series with the voltage source. This source impedance increases with decreasing film capacitance and decreasing frequency of operation. The source impedance combined with load resistance (such as the input resistance of an oscilloscope) forms a voltage divider. As the ratio of the load

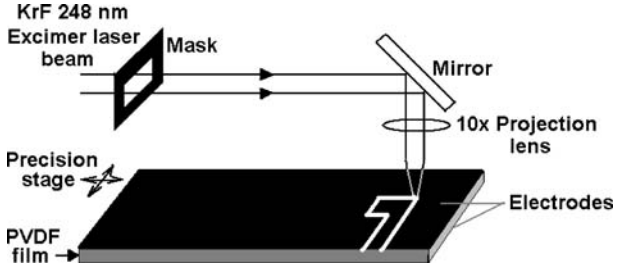

Fig. 1 Electrode patterning of PVDF piezoelectric film using excimer laser micro-machining technique

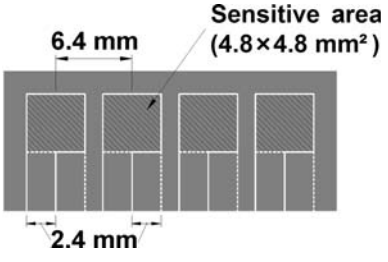

Fig. 2 Layout of the PVDF array sensor. *Dashed lines* indicate the patterning on the reverse side electrode

resistance to the source impedance is decreased, the output voltage is reduced, so called the *loading effect*. In the case of large sensitive area (and hence a high capacitance or low source impedance), a PVDF sensor can be directly connected to electronic devices without considerations of special interface. However, the sensing elements designed in this work are so small that the capacitance of each unit (including the connecting cable) is only about 100 pF (at 2 kHz). With 1 MΩ load resistance, the low-end cut-off frequency is as high as 1.6 kHz; all output signals below this frequency will be significantly reduced.

To solve this problem, we design a buffer circuit (Fig. 3a) for each of the sensing elements using an operational amplifier (AD843JR, Analog Devices, Inc.). The amplifier has very high input resistance (about 10 GΩ) and, therefore, eliminates the loading effect. The buffer circuit also converts the high output impedance of the piezo element into low impedance (about 12 Ω) and thus minimizes the signal loss and noise through the cable. In order to reduce the noise from multiple ground loops, all of the circuit grounds are joined together. To test the bandwidth of the buffer circuit, we use an 80 MHz function generator (Agilent 33250A) as input and record the output signal by a 100 MHz digital oscilloscope (Tektronix TDS 3014). Figure 3b shows its large signal (7.5 V peak to peak) frequency response. A flat unity-gain-bandwidth up to 20 MHz is obtained.

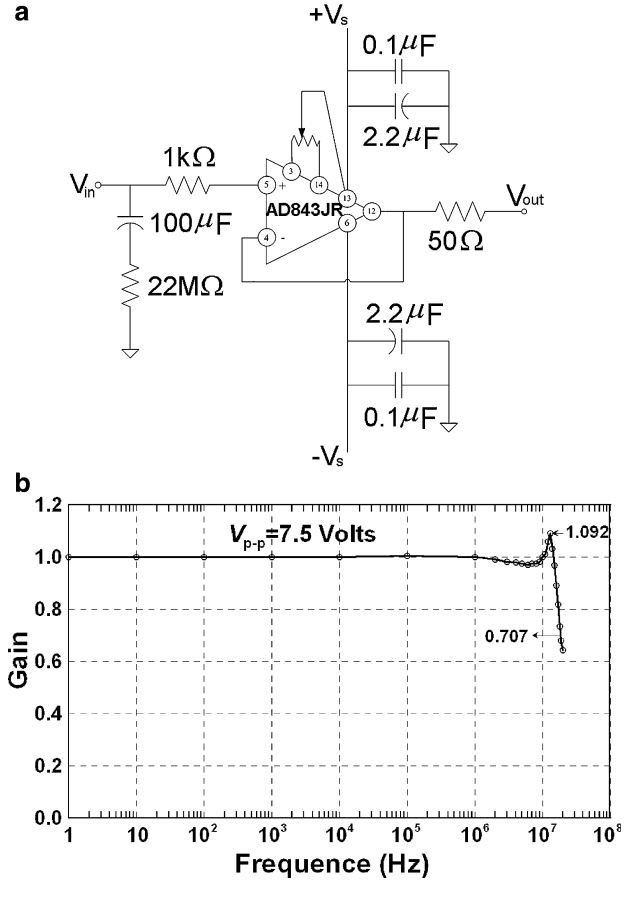

Fig. 3 **a** Buffer circuit for PVDF sensor. V_{in} is the signal from the sensor, V_{out} is the signal output to oscilloscope, V_s is supply voltage (±15 V); **b** bandwidth of large signal unity gain of the circuit

3 Dynamic calibration of PVDF sensor array

3.1 Crosstalk of the sensors

To estimate the crosstalk between the sensing elements, we drop a steel ball of 8 mm in diameter on one of the elements and monitor the output signals from the element and its neighbors. Impact signals from the dropping ball are illustrated in Fig. 4. Relative comparison of the signal amplitude shows an insignificant crosstalk level less than 2%.

3.2 Dynamic calibration using a gas shock tube

Dynamic calibration of the array sensor is accomplished using a gas shock tube of inner diameter of 50.8 mm (PCB Model 901A10, PCB Piezotronics Inc.). As shown in Fig. 5, compressed gas is pressurized in the driver section until the aluminum diaphragm bursts, sending a shock wave into the test section. The shock wave is reflected at the end steel plate on which the array sensor is attached. Depending on the driven gas and the thickness of the diaphragm, the facility can produce reflected shock waves from 20.7 kPa to more than 6.9 MPa with rising time of nanoseconds and, therefore, is quite useful for determining sensor resonance characteristics.

Applying the one-dimensional gas dynamic conservation equations, the amplitude of the reflected shock wave, p_r, can be expressed as

$$\frac{p_r}{p_0} = \frac{\left(8M_s^2 - 2\right)\left(7M_s^2 - 1\right)}{6\left(M_s^2 + 5\right)} \tag{1}$$

where p_0 is the pressure ahead of the incident shock wave (the barometric pressure), $M_s \equiv u_s/c$ is the incident

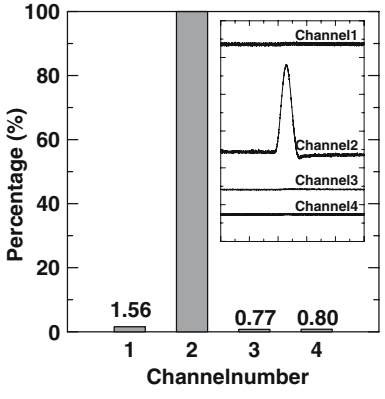

Fig. 4 Coupling between array of sensors. Inset displays signals from steel ball dropping directly on the sensor labeled as *channel 2*

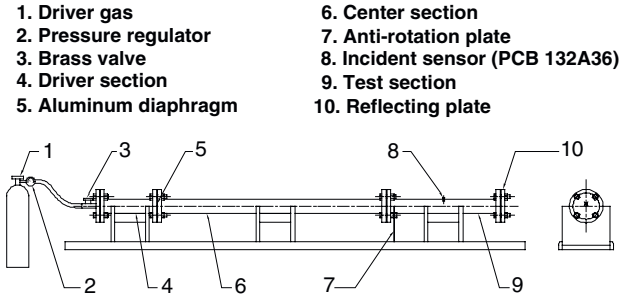

Fig. 5 Gas shock tube (PCB 901A10) for dynamic calibration of PVDF array sensor. The sensor array is attached on the reflecting plate

shock Mach number, u_s is the incident shock wave velocity and c is the sound speed in the air which is function of temperature. The incident shock speed is determined from the distance (304.63 mm) between the incident sensor (PCB 132A36) and the test sensor divided by the time difference (typical of several hundred microseconds depending on the strength of the shock) between the output signals of them. Based on the fast rise time (<0.2 μs) of the incident sensor and the instruments for measuring the atmospheric pressure and temperature, the accuracy of p_r is approximately $\pm 1.5\%$.

Typical shock loading signals of the array sensor are presented in Fig. 6a. Dynamic characteristics of these signals are almost identical, representing good uniformity of the sensor characteristics. The average rising time of these signals is 31 ns, corresponding roughly to a bandwidth of 11.3 MHz. Calibration results of the array sensor are demonstrated in Fig. 6b, showing an average sensitivity of 1.015×10^5 Pa/V about half of the value provided by the supplier (2.222×10^5 Pa/V). It is noteworthy that the supplier's sensitivity is estimated in terms of the thickness-mode piezo coefficient, g_{33} (0.18 V/m per Pa), of the PVDF film and, therefore, is for ideal mechanical and electrical boundary conditions. Actually, the sensitivity is expected to change due to, for example, the mismatch in acoustic impedance between the PVDF film and the metal electrodes and the attenuation of the adhesive layer used for bonding the sensor on the backing.

It is well known that the backing material has important effects on the response frequency of a piezoelectric polymer ultrasonic transducer. Brown (2000) demonstrated that for a backing material with acoustic impedance close to (or lower than) that of the polymer, the transducer operates in the half wavelength resonance frequency:

$$f_{\lambda/2} = \frac{c_p}{2t} \tag{2}$$

where c_p = speed of sound in the PVDF polymer (≈2,200 m/s) and t = thickness of the piezoelectric film (25 μm in this study). With the increase of the backing

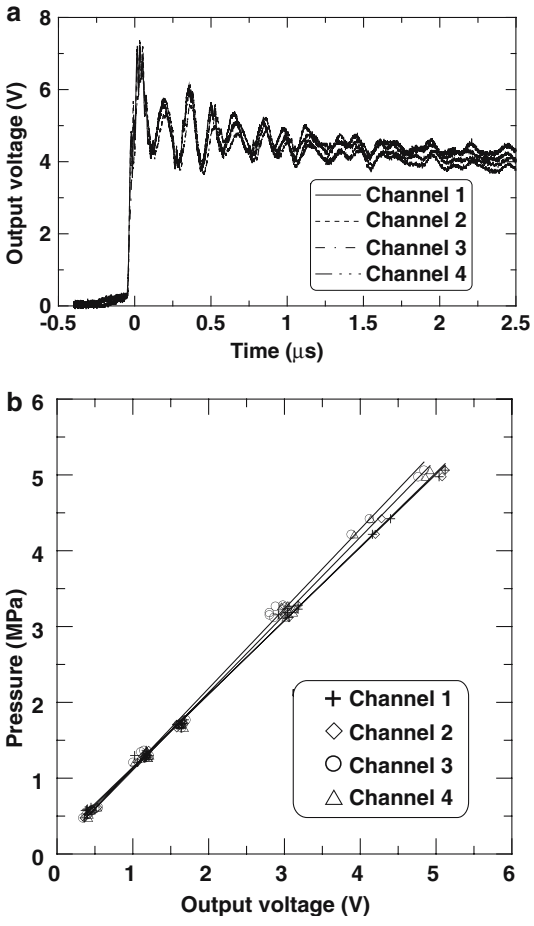

Fig. 6 **a** Typical shock wave loading signals of the array sensor; **b** calibration results

acoustic impedance the peak resonant frequency of the transducer transits to the quarter wavelength mode; the factor 1/2 in Eq. (2) is then replaced by 1/4. In practice, an epoxy adhesive layer is usually used to adhere the piezoelectric film to the backing material (the acoustic impedance and the longitudinal acoustic velocity of most epoxies are close to that of PVDF). Using an adhesive layer between the film and a high impedance backing material (such as a metal substrate) can change the mechanical resonant frequency of the transducer to a new value (see Brown 2000 and the references therein). In our experiment the piezoelectric film is adhered to an aluminum backing using a 25.4 μm thick two-sided acrylic adhesive tape (3M 9641P). Since the thickness of the adhesive layer almost equals the thickness of the piezoelectric film, the film should resonate in the $\lambda/4$ mode (at 11 MHz) of a 50 μm thick stack. When the attenuation within the PVDF film and the effect of electrodes are accounted for, this frequency is expected to drop further (see Brown 2000). Theoretical analysis of the characteristics of the PVDF sensor is beyond this work. However, the ringing following the fast rising shock front in Fig. 6a reveals a resonance frequency of 6.3 MHz.

4 Measurements of bubble collapse pressure

4.1 Experimental setup

A schematic diagram of the experimental setup is shown in Fig. 7. Cavitation bubble is generated in de-ionized water (made by a reverse osmosis machine) by discharging a capacitor (1.2 μF) across a pair of tungsten electrodes (1 mm in diameter). The electrical conductivity of the RO water is 1.5 μS/cm (measured using WTW LF330 conductivity meter). The bubble generator is capable of maximum capacitor charge of 10 kV and is equipped with a discharge gap switch, which is controlled by an external trigger signal. The electrodes are mounted on a two-axis precision displacement stage. The gap distance of the electrodes and the distance from the gap to the solid boundary, L, can be adjusted precisely by micrometers. The maximum radius of the cavitation bubble, R_{max}, is measured directly using a high-speed CCD camera (Kodak SR-Ultra, maximum framing rate of 10,000 frames/s). By careful control of the water conductivity, electrode gap distance, and the discharge voltage, cavitation bubbles of a quite stable size can be realized. Figure 8 shows the variation of maximum bubble diameter in consecutive spark discharges for charge voltage of 5,000 V and initial gap distance of 0.3 mm. Due to the high temperature wear of the electrodes, the gap distance might be varied and, consequently, R_{max} changes. This effect is obvious in Fig. 8 as the consecutive discharge number is less than ten. A stable region of maximum bubble size exists and is adopted in our experiments. Beyond this region, the electrode gap distance is readjusted and the same procedures are repeated. By keeping R_{max} constant, various values of the stand-off parameter, $\gamma = L/R_{max}$, can be set by adjusting the distance L.

Right under the gap of the electrodes, the PVDF sensor array is attached to the solid boundary. The array of sensors covers a range of 24 mm, wider than the size of the cavitation bubble under its maximum expansion condition. The signals from the sensors are simultaneously acquired through a four-channel digital oscilloscope (Tektronix TDS 3014, bandwidth 100 MHz, maximum sampling rate 1.25 Gsamples/s).

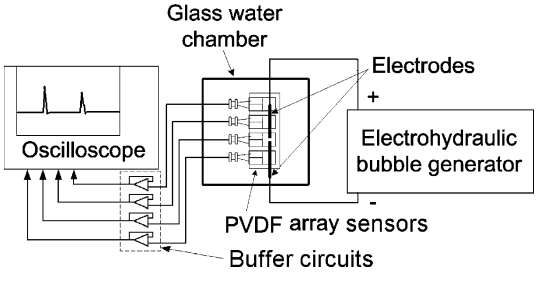

Fig. 7 Experimental setup

4.2 Results and discussion

Figure 9a displays the signal traces from the array of sensors for a relative large value of $\gamma = 2.8$. The two serial spikes on each channel correspond to the impulsive loadings due to the first and second collapses of the bubble, respectively. Figure 9b shows a magnification of the pulses generated by the first bubble collapse on which the current work concentrates. The pressure pulses measured by all of the four sensors exhibit a relatively slow (within 2 μs) pressure rise followed by a fast rising shock front, a typical feature of the acoustic transient generated by cavitation bubble collapse (see, for example, Vogel et al. 1989). The shock first reaches channel 3 with a rise time of 130 ns and duration of 590 ns and propagates outwardly. Broadening of the pressure profile is obvious from channel 2 (or channel 4) and channel 1, consistent with the finite-amplitude wave propagation theory of Cole (1948) and Esipov and Naugol'nykh (1972).

The speed of the shock can be calculated based on the sketch of the geometry shown in Fig. 10 and is given by

$$V_s = V_p \cos\alpha = \frac{dx}{dt}\frac{x}{\sqrt{L^2 + x^2}} \tag{3}$$

in which V_s is the speed of the spherical shock wave, V_p is the moving speed of the intersection points (a circle) of the spherical and the reflecting shock waves, x is the position of the moving points and L is the distance from the shock emission center to the boundary ($L = \gamma R_{max} = 27.5$ mm). If we assume that V_s is constant, Eq. (3) can be integrated to obtain

$$V_s = \frac{\left|\sqrt{L^2 + x_2^2} - \sqrt{L^2 + x_1^2}\right|}{|t_2 - t_1|} \tag{4}$$

in which x_2 and x_1 correspond to the locations of the neighboring sensors and $t_2 - t_1$ is the time difference between the spikes registered by these sensors. If we assume that the shock emission center is exactly above the sensor labeled as channel 3 in Fig. 9 (the migration of the collapsing bubble toward the boundary is neglected), the speed of the shock can then be estimated based on the spacing between the sensors (refer to Fig. 2) and

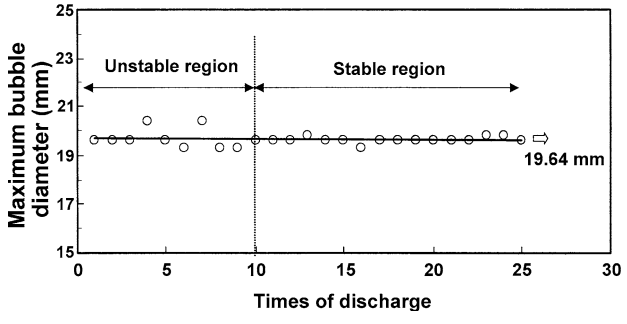

Fig. 8 Variation of maximum bubble diameter with the number of serial spark discharges

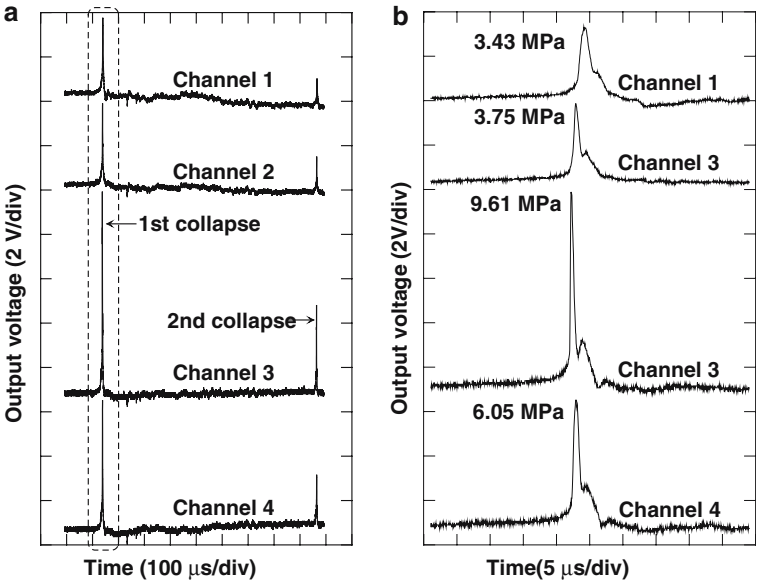

Fig. 9 Impulsive signals generated by cavitation bubble collapse for $\gamma = 2.8$: **a** showing first and second bubble collapse; **b** first bubble collapse at higher resolution. Value of maximum pressure on each channel is as indicated

time difference between the spikes shown in Fig. 9b. The speed of the spherical shock wave as it propagates from channel 2 to channel 1 ($|t_2 - t_1| = 1.2$ μs) is calculated as 1754 m/s. Note that Eq. (4) cannot be applied between channel 3 and channel 2 (or channel 4) due to the geometrical divergence at channel 3; V_p in Eq. (3) is unbounded as α equals to 90°.

By decreasing the value of γ to 1.2 (Fig. 11), the sensor of channel 3 (which is placed right under the gap of the electrodes) first experiences a gentle increase of pressure during a time lasting approximately 20 μs and then a fast-rising and short duration shock pulse is recorded and is followed by a second shock spike. The two consecutive shock waves overtake each other (see channel 2 and channel 4) and coalesce into a single wave form as they propagate to channel 1. It is well known that, for this value of γ, a high-speed liquid jet penetrates the bubble before it is compressed to minimum volume (see Tomita and Shima 1986; Shaw et al. 1996; Tong et al. 1999 among others). The impingement of the jet on the solid boundary produces a much longer lasting signal compared to the shock waves. Recently, the high-speed photographic record (5 million frames/s) taken by Brujan et al. (2002) demonstrated that, for $\gamma = 1.1$, the

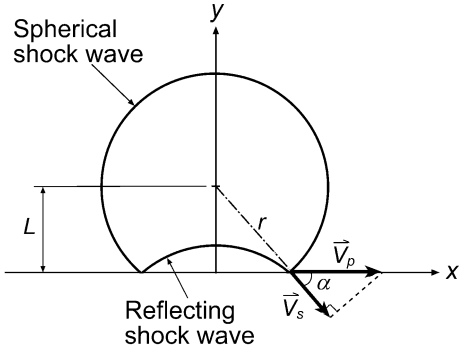

Fig. 10 Notation used for calculating shock speed: V_s is the propagating speed of the spherical shock wave, V_p is moving speed of the intersection points of the spherical and the reflecting shock waves

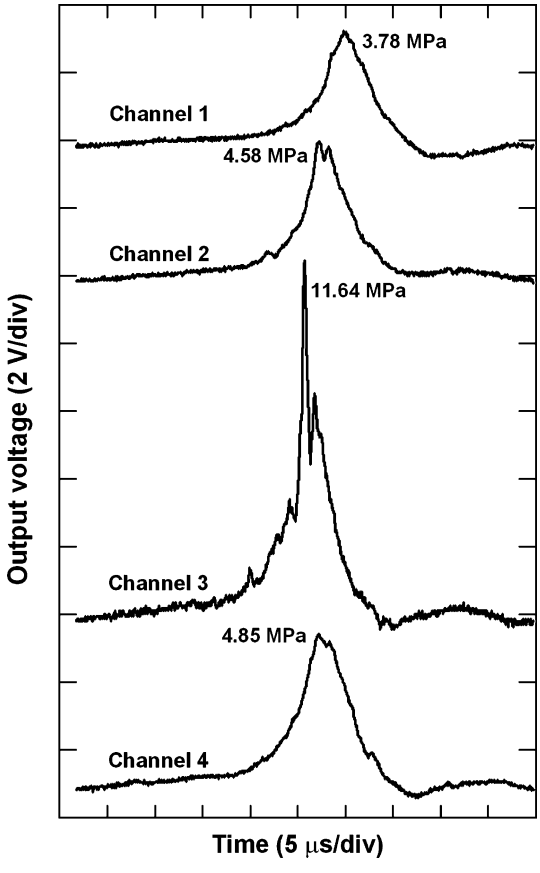

Fig. 11 Highly resolved impulsive signals due to the first collapse of cavitation bubble for $\gamma = 1.2$. Value of maximum pressure on each channel is as indicated

bubble becomes toroidal after jet penetration. A shock wave is emitted due to the collapse of the part of the bubble far from the boundary and the bubble splits into two toroidal cavities. About 0.2 μs later, a second shock wave is emitted from the splitting position. The sensor outputs shown in Fig. 11 confirm these observations but the time lag of the second shock wave is about 1 μs. However, it should be mentioned that the bubble in the present work is about six times larger than that of Brujan et al. and, therefore, should have a larger temporal scale of events.

Figure 12 displays the pressure signals induced by the first bubble collapse at $\gamma = 0.9$. According to Tomita and Shima (1986), the liquid jet impacts on the solid boundary earlier than the case of $\gamma = 1.2$. Examining the signal trace on channel 3, it is noted that the jet hits the boundary approximately 40 μs before the first shock spike appears, in comparison to 25 μs when $\gamma = 1.2$, thus in agreement with Tomita and Shima's observations. Following the jet impact, a train of at least five fast-rising spikes is discriminable. Brujan et al. (2002) recently highlighted the source of these spikes. For $\gamma = 0.9$, they pictured emission of multiple shock waves after the liquid jet penetrates the bubble, splashes away from the solid boundary, and leads to the formation of two toroidal cavities split from the main bubble; the torus farther from the boundary disintegrates into several parts, collapses separately, and emits several different shock waves.

Figure 13 shows the sensor outputs for the small value of $\gamma = 0.36$. The signal of channel 3 in Fig. 13 is similar to that in Fig. 12; a liquid jet impacts on the surface and then several shock waves are recorded. However, since the liquid film between the bubble and the boundary is now very thin, the jet impact is more direct and, therefore, the long-duration jet signal is much pronounced. Another interesting difference between Fig. 13 and Fig. 12 is the relative timing of the signals among sensors. In Fig. 13, channels 2, 3, and 4 receive impulses almost simultaneously. Recent study (see, for example, Philipp and Lauterborn 1998; Lindau and Lauterborn 2003) has demonstrated that, for such a small value of γ, the liquid jet sets up an unstable torus bubble right on the solid surface. Multiple simultaneous collapses happen along the major axis of the torus, which might cover the area of the sensing elements corresponding to the above three channels.

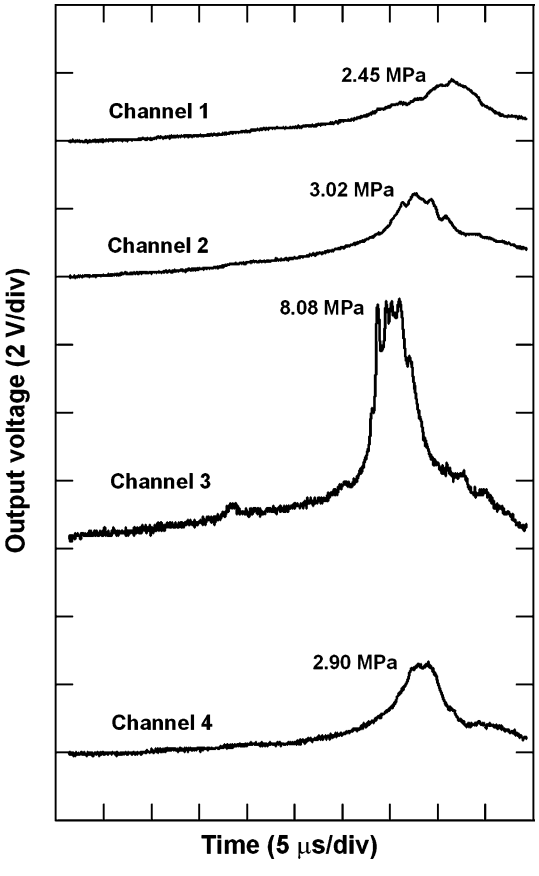

Fig. 12 Highly resolved impulsive signals due to the first collapse of cavitation bubble for $\gamma = 0.9$. Value of maximum pressure on each channel is as indicated

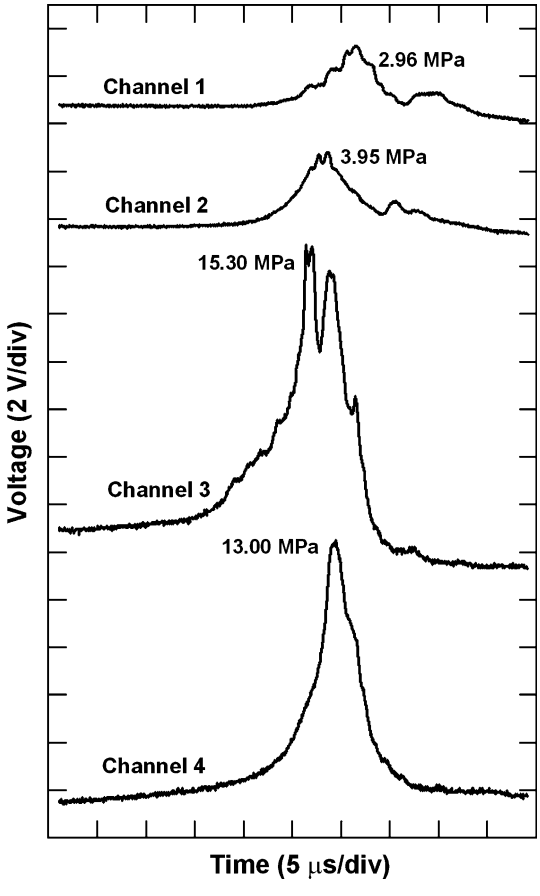

Fig. 13 Highly resolved impulsive signals due to the first collapse of cavitation bubble for $\gamma = 0.36$. Value of maximum pressure on each channel is as indicated

5 Conclusion

The development of an array of PVDF piezoelectric pressure sensors is demonstrated in this work. Using an excimer laser micro-machining technique, the metal electrodes on each side of a thin (25 μm) PVDF film can be patterned independently and accurately. Overlapping isolated electrodes from both sides of the film forms the active area of each sensor. Based on the current technique, a two-dimensional array of sensors can be easily realized although a one-dimensional case is demonstrated here.

Dynamic characteristics of the array sensor are examined using a dropping-ball and a gas shock tube techniques. The dropping-ball test provides the crosstalk level between the sensors, which is shown less than 2%. The gas shock tube allows the sensors be calibrated simultaneously and uniformly. Output signals from the dynamic shock loading indicate a good uniformity of the sensor array with an average rise time as fast as 31 ns; therefore, very suitable for measuring impulsive pressure fields as induced by cavitation bubble collapse.

Although many research efforts have focused on the flow dynamics and material damage associated with cavitation bubble collapse, measurement of the impulsive pressures due to cavitation is still a very challenging problem. The complexity comes mainly from two sources. First, the duration of a typical pressure pulse is very short; hence the pressure sensor must be very broadband to accurately reproduce the sudden rise of the pressure. PVDF piezoelectric film has been shown to be a potential sensor material in this respect. However, care must be taken to consider the factors that can lower the response frequency, including the substrate material, the electrodes, and the bonding materials. Secondly, the sensitive surface of the sensor must be smaller than the real impact size associated with cavitation bubble collapse; otherwise the measured quantity is actually an underestimated equivalent pressure which would give the same output as if it were uniformly applied to the entire sensitive surface. In this study the sensitive area (4.8 mm×4.8 mm) of the sensor is probably several orders of magnitude larger than the excitation area of bubble collapse. Theoretically, if one knew the excitation area, the impulsive pressure can be easily obtained by multiplying an area correction factor. For example, for a 10 μm diameter impact site, a correction factor of 2.9×10^5 would be required. However, as shown by Philipp and Lauterborn (1998), the erosion pattern and pit sizes (both directly related to the impact area) of single cavitation bubbles depend on the parameter γ and the maximum bubble radius in an extremely complicated way; quantitative information about the impact area for the range of γ of present study is still incomplete. Based on the laser micro-machining technique in this study, the sensitive area of the sensor can be much further reduced to increase the spatial resolution, on which we are currently working.

Signal outputs of the array of sensors indicate that the bubble collapse always generates shock waves no matter what value of the stand-off parameter γ is. For a relative large value of $\gamma = 2.8$, only one shock wave is recorded. The speed of the shock can be calculated based on the spacing and the time difference of the signals between the sensors. As the bubble inception center is brought closer to the boundary ($\gamma \leq 1.2$), the array sensor is subjected to several distinct pressure stresses, which are different in intensity and duration. Signals from the sensor right under the bubble inception center show that the main pressure loading consists of multiple hydrodynamic shock waves. These fast rising and short duration shock pulses are superimposed on a longer lasting pressure stress resulting from the jet flow. The shock waves overtake each other and tend to coalesce into a single wave form as they propagate outward.

When the bubble is very close to the boundary ($\gamma = 0.36$) three of the sensors receive pressure pulses almost simultaneously. This result may be explained by the recent photographic observations of Philipp and Lauterborn (1998) and Lindau and Lauterborn (2003). For $\gamma < 0.6$ they observed the liquid jet sets up an unstable torus bubble right on the solid surface. Multiple simultaneous collapses and rebounds happen along the major axis of the torus. Lindau and Lauterborn (2003) also reported the quantitative dependence of the normalized (by R_{max}) radius of the major torus on the stand-off parameter. Further investigations are currently planned to determine the collapsing pressure of the torus bubble by distributing the sensor array along the major radius of the torus.

Acknowledgments The authors are grateful to Dr G.N. Sankin for useful discussions on the estimation of the shock speed. National Science Council, Taiwan sponsored this work under contract No. NSC 91-2212-E-006-154.

References

Arndt REA, Paul S, Ellis CR (1997) Application of piezoelectric film in cavitation research. J Hydr Engr 123:539–548

Brennen CE (1995) Cavitation and bubble dynamics. Oxford University Press, New York, pp 66–80

Brown LF (2000) Design considerations for piezoelectric polymer ultrasound transducers. IEEE Trans Ultrasound, Ferroelect, Freq Contr 47:1377–1396

Brujan EA, Keen GS, Vogel A, Blake JR (2002) The final stage of the collapse of a cavitation bubble close to a rigid boundary. Phys Fluids 14:85–92

Cole RH (1948) Underwater explosions. Princeton University Press

Esipov IB, Naugol'nykh KA (1972) Expansion of a spherical cavity in a liquid. Soviet Phys Acoust 18:194–197

Harris GR, Lewin PA (1999) Ultrasonic exposimetery. In: Webster JG (ed) Encyclopedia of electrical and electronics engineering, vol 22. Wiley, New York, pp 634–646

Jones IR, Edwards DH (1960) An experimental study of the forces generated by the collapse of transient cavities in water. J Fluid Mech 7:596–609

Lindau O, Lauterborn W (2003) Cinematographic observation of the collapse and rebound of a laser-produced cavitation bubble near a wall. J Fluid Mech 479:327–348

Philipp A, Lauterborn W (1998) Cavitation erosion by single laser-produced bubbles. J Fluid Mech 361:75–116

Shaw SJ, Jin YH, Schiffers WP, Emmony DC (1996) The interaction of a single laser-generated cavity in water with a solid boundary. J Acoust Soc Am 99:2811–2824

Shaw SJ, Schiffers WP, Gentry TP, Emmony DC (2000) The interaction of a laser-generated cavity with a solid boundary. J Acoust Soc Am 107:3065–3072

Soyama H, Lichtarowicz A, Momma T, Williams EJ (1998) A new calibration methods for dynamically loaded transducers and its application to cavitation impact measurement. ASME J Fluids Eng 120:712–718

Tomita Y, Shima A (1986) Mechanisms of impulsive pressure generation and damage pit formation by bubble collapse. J Fluid Mech 169:535–564

Tong RP, Schiffers WP, Shaw SJ, Blake JR, Emmony DC (1999) The role of 'splashing' in the collapse of a laser-generated cavity near a rigid boundary. J Fluid Mech 380:339–361

Vogel A, Lauterborn W (1988) Acoustic transient generation by laser-produced cavitation bubbles near solid boundaries. J Acoust Soc Am 84:719–731

Vogel A, Lauterborn W, Timm R (1989) Optical and acoustic investigations of the dynamics of laser-produced cavitation bubbles near a solid boundary. J Fluid Mech 206:299–338